CHEMISTRY OF MATERIALS

pubs.acs.org/cm

Article

Phase Diagram and Cation Dynamics of Mixed $MA_{1-x}FA_xPbBr_3$ Hybrid Perovskites

Mantas Šimėnas,* Sergejus Balčiūnas, Šarūnas Svirskas, Martynas Kinka, Maciej Ptak, Vidmantas Kalendra, Anna Gągor, Daria Szewczyk, Adam Sieradzki, Robertas Grigalaitis, Aron Walsh, Mirosław Mączka, and Jūras Banys

Cite This: *Chem. Mater.* 2021, 33, 5926−5934

Read Online

ACCESS | Metrics & More | Article Recommendations | Supporting Information

ABSTRACT: Mixing of molecular cations enhances the optoelectronic properties and stability of hybrid lead halide perovskites. Here, we use a multitechnique approach to determine the phase diagram and molecular cation dynamics of mixed methylammonium-formamidinium $MA_{1-x}FA_xPbBr_3$ ($0 \le x \le 1$) hybrid perovskites. The calorimetric, ultrasonic, and X-ray diffraction experiments show a substantial suppression of the structural phase transitions and stabilization of the cubic phase upon mixing. We use the broad-band dielectric and Raman spectroscopies to study the MA and FA cation dynamics in these compounds. The broad-band dielectric spectroscopy indicates the absence of the MA cation ordering and a gradual increase of the rotation barrier upon mixing. The room-temperature dielectric permittivity substantially decreases as the fraction of the FA cations is increased. No significant changes of the permittivity are detected at temperatures, where the dielectric relaxations are absent. We also observe weak signatures of a dipolar glass phase for the intermediate mixing levels. The Raman spectroscopy supports the dielectric results and reveals additional subtle information about the FA cation dynamics.

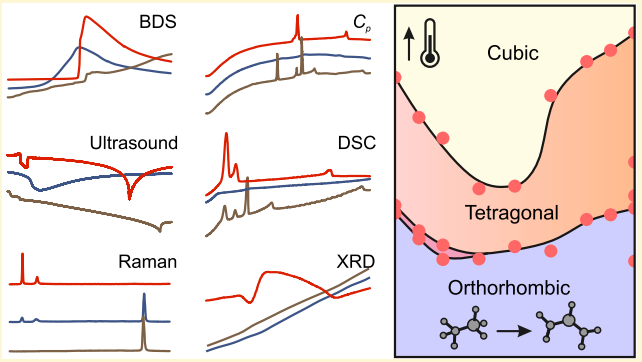

INTRODUCTION

Methylammonium (MA, $CH_3NH_3^+$) lead halide perovskites $MAPbX_3$ (X = I, Br, Cl) have attracted extraordinary attention of the scientific community as highly efficient materials for photovoltaic applications.[1−3] The power conversion efficiency of solar cells based on these hybrid compounds has demonstrated a remarkable boost in the past decade and currently exceeds 25%.[4−9] A high performance of these materials results from the interplay of several physical factors including a large absorption coefficient,[10] optimal band gap,[11] long carrier diffusion lengths[12] and lifetime,[13] low exciton binding energy,[14] and defect tolerance.[15]

The best efficiency and stability of hybrid perovskite solar cells are achieved by mixing of the A-site cations.[16−20] The most popular alternatives to MA are formamidinium (FA, $HC(NH_2)_2^+$) and Cs^+, although less popular cations such as Rb^+,[21] dimethylammonium (DMA),[22−24] and methylhydrazinium[25,26] are also gaining attention. Mixing of the A-site cations is also frequently used to stabilize the desirable photoactive black phases of $FAPbI_3$ and $CsPbI_3$ perovskites that otherwise crystallize into the photoinactive yellow phases at room temperature.[16,27,28]

Despite an extensive use of mixed lead halide perovskites in solar cell fabrication,[16,17,19,29] there are, by far, a less number of studies that provide a detailed picture of the structural phase transitions, phase diagrams, and cation dynamics that are tightly related to the attractive properties of these materials. Several recent works reported phase diagrams of $FA_{1-x}Cs_xPbX_3$ (X = I, Br)[30,31] and $MA_{1-x}Cs_xPbI_3$[32] perovskites, where the latter compounds demonstrated signatures of an electric dipole (orientational) glass phase. Such a phase was also observed by the broad-band dielectric spectroscopy in our recent investigation of mixed $MA_{1-x}DMA_xPbBr_3$ compounds, where MA frustration is caused by a local lattice deformation due to neighboring DMA cations.[24] Another study determined the phase diagram of $MA_{1-x}FA_xPbI_3$ perovskites and suggested that a tetragonal symmetry dominates for higher values of x.[33] This observation is in contrast to work by Mohanty et al.[34] who instead reported a cubic superstructure.

In this work, we use a multitechnique approach to determine previously uncharted phase diagram of $MA_{1-x}FA_xPbBr_3$ ($0 \le x$

Received: March 12, 2021
Revised: July 9, 2021
Published: July 26, 2021

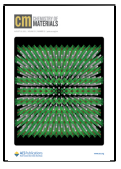

≤ 1) and probe the cation dynamics in this mixed perovskite family. $MAPbBr_3$ was extensively studied before, and its phase behavior is rather well known. This compound exhibits three structural phase transitions at 236, 153, and 144 K, which correspond to cubic ($Pm\bar{3}m$) → tetragonal-I ($I4/mcm$) → tetragonal-II ($P4/mmm$) → orthorhombic ($Pnma$ or $Pna2_1$) transitions, respectively.[35−38] The phase transitions and cation dynamics in $FAPbBr_3$ are less understood. Recent studies reported two transitions at about 266 K and 153 K, which correspond to cubic ($Pm\bar{3}m$) → tetragonal ($P4/mbm$) → orthorhombic ($Pnma$) symmetry lowering.[39−41] Three additional isostructural transitions were observed at 182, 162, and 118 K that involve changes of the FA cation dynamics and are not resolved crystallographically.[30,42] A substantial degree of disorder of FA cations was found even at 10 K temperature.[41]

Our results show that mixing of these compounds significantly lowers the temperatures of the structural phase transitions, resulting in stabilization of the cubic phase. We observe drastic perturbations of the cation dynamics and long-range order upon mixing, which are reflected as the pronounced changes in the dielectric response. We also observe weak indications of a dipolar glass phase for the intermediate mixing levels.

EXPERIMENTAL DETAILS

Sample Synthesis. Single crystals of $MA_{1-x}FA_xPbBr_3$ (x = 0, 0.1, 0.2, 0.35, 0.5, 0.65, 0.8, 0.9, and 1) were grown using antisolvent vapor-assisted crystallization. In the typical synthesis, 2 mmol $PbBr_2$ was added to a mixture containing 10 mmol hydrobromic acid, 5 mL of acetonitrile, and an appropriate amount of formamidinium acetate and methanol solution of methylamine (2 mmol). Then, dimethyl sulfoxide (DMSO) was added to the prepared solution under stirring until complete dissolution of the orange precipitate (~1 mL). The clear solution was transferred into a glass vial, which was placed in a second larger glass vial containing methyl acetate. The lid of the outer vial was thoroughly sealed, but the lid of the inner vial was loosened to allow diffusion of the methyl acetate into the precursor solution. Orange crystals were harvested after 5−7 days, washed with acetonitrile, and dried at room temperature.

DSC. The differential scanning calorimetry (DSC) experiments of powder samples were performed using a Mettler Toledo DSC-1 calorimeter with a high resolution of 0.4 μW. Nitrogen was used as a purging gas, and the heating/cooling rate was 5 K/min. Mass of the samples (in mg) was as follows: 38.68 (x = 0), 65.17 (x = 0.1), 76.44 (x = 0.2), 54.05 (x = 0.35), 48.29 (x = 0.5), 43.84 (x = 0.65), 29.13 (x = 0.8), 50.36 (x = 0.9), and 62.22 (x = 1).

XRD. Lattice parameters of $MA_{1-x}FA_xPbBr_3$ were calculated from the single-crystal X-ray diffraction (XRD) data, collected using an Xcalibur Atlas diffractometer operating with Mo Kα radiation and a Cryostream 800 low-temperature attachment from OxfordCryosystems. Cubic restraints were used for x = 0.5, 0.65, 0.8, 0.9, and 1 samples due to the presence of a pseudocubic structure in the entire temperature range. For x = 0, 0.1, 0.2, and 0.35 compositions, due to the significant lattice distortion, the orthorhombic restraints were implemented.

Powder XRD (PXRD) measurements were performed on an X'Pert PRO powder diffractometer operating with Cu Kα radiation.

Heat Capacity. Heat capacity at constant pressure, C_p, of all samples was measured in a temperature range of 1.8−275 K using a thermal relaxation technique in the heat capacity option of the physical property measurement system (PPMS). The typical accuracy of the system is better than 1% for temperatures above 100 K and slightly diminishes at lower temperatures. For the measurements, the single-crystal samples were used with sample mass varying from 4.1 to 6.8 mg.

Dielectric Spectroscopy. Broad-band dielectric spectroscopy experiments were performed in three different frequency bands. (i) 20 Hz−1 MHz band: measurements of capacitance and loss tangent with HP4284A and Solartron Modulab XM MTS LCR meters. The flat capacitor model was implemented to calculate the complex dielectric permittivity. (ii) 1 MHz−1 GHz band: the complex reflection coefficient was measured with an Agilent 8714ET vector network analyzer. The multimode capacitor model was used to calculate the complex dielectric permittivity.[43,44] (iii) 26−50 GHz band (only x = 0 sample): the scalar transmission and reflection coefficients were measured in a waveguide system. The sample was perpendicularly centered on a wider wall of the waveguide. The dimensions of the waveguide were chosen such that only the fundamental H_{10} mode can propagate. Transmission/reflection coefficients were measured with a scalar network analyzer Elmika R2400. A detailed description of the experimental setup can be found in ref 45. Temperature-dependent dielectric spectra were measured on cooling at a rate of 1 K/min. Temperature was determined with a Keithley Integra 2700 multimeter, a T-type thermocouple, and a 100 Ω platinum resistor. The uncertainty of the sample size and imperfect calibration of the measurement setups results in about 3% error of systematic overestimation/underestimation of the dielectric permittivity.

Raman Spectroscopy. Room-temperature Raman spectra were measured using a Bruker FT100/S spectrometer with YAG:Nd^{3+} laser excitation (1064 nm). Temperature-dependent Raman spectra of single-crystal samples were obtained using a Renishaw InVia Raman spectrometer equipped with a confocal DM 2500 Leica optical microscope, a thermoelectrically cooled CCD as a detector, and a diode laser operating at 830 nm. To obtain information on the low-wavenumber modes, additional measurements were performed on the same instrument using an eclipse filter. The temperature was controlled using a Linkam cryostat cell. The spectral resolution was 2 cm^{-1}.

Light Absorption. Diffuse reflectance spectra were obtained at room temperature on powder samples prepared by grinding single crystals in a mortar. The measurements were performed using a Varian Cary 5E UV−VIS−NIR spectrophotometer and a Praying Mantis diffuse reflectance accessory.

Ultrasonic Measurements. The ultrasonic velocity and attenuation data of single-crystal samples were obtained using a computer-controlled RITEC RAM-5000 pulse-echo ultrasonic measurement system from the phase shift and amplitude of the received signal. $LiNbO_3$ transducers were used for the excitation and detection of longitudinal ultrasonic waves at 10 MHz. Typical sample thickness was 2−3 mm, and the heating/cooling rate was kept below 1 K/min. Silicon oil was used between the sample, quartz buffer rods, and transducers to maintain acoustic bonds in the whole studied temperature range.

RESULTS AND DISCUSSION

Our study was carried out on the mixed $MA_{1-x}FA_xPbBr_3$ perovskite crystals with x = 0, 0.1, 0.2, 0.35, 0.5, 0.65, 0.8, 0.9, and 1. Initial sample characterization was performed using Raman spectroscopy, which revealed a monotonous increase (decrease) in FA (MA) Raman band intensity with increasing x (see Figure S1, Supplementary Information). The PXRD patterns of the mixed compounds exhibited no reflections of secondary or unmixed phases (Figure S2). The light absorption measurements revealed a red shift of the band gap upon an increase in x (Figure S3) in agreement with other studies.[19,46] All of these experiments demonstrate successful incorporation and mixing of the cations.

To characterize the phase transition behavior and build a phase diagram of $MA_{1-x}FA_xPbBr_3$, we performed measurements of heat capacity C_p, DSC, ultrasonic propagation, dielectric spectroscopy, and single-crystal XRD. Such a combination of experimental techniques proved to be a very powerful approach to detect the transition anomalies and distinguish them from the experimental artifacts. For the

https://doi.org/10.1021/acs.chemmater.1c00885
Chem. Mater. 2021, 33, 5926−5934

$MAPbBr_3$ (x = 0) sample, the C_p, DSC (Figure 1), and ultrasonic (Figure S4) experiments revealed three anomalies at

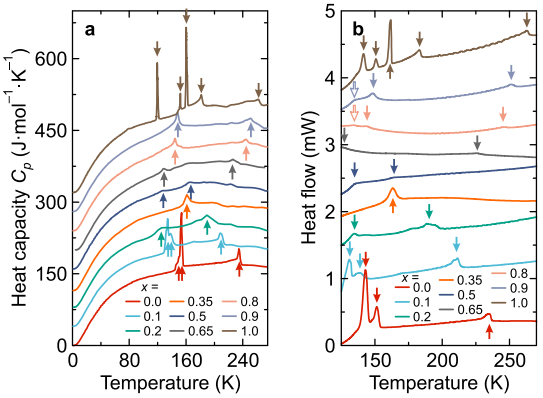

Figure 1. Temperature dependence of the (a) heat capacity and (b) DSC traces of $MA_{1-x}FA_xPbBr_3$ perovskites obtained on cooling. The curves are offset by an arbitrary shift for clarity. The filled arrows indicate phase transition anomalies. The empty arrows in (b) mark experimental artifacts due to the change in the cooling rate.

about 236, 154, and 146 K, which correspond to the cubic → tetragonal-I → tetragonal-II → orthorhombic phase transitions, respectively.[35−38] As the FA fraction increased to x = 0.35, the phase transitions gradually shifted to lower temperatures and became significantly broader. This indicates that mixing perturbs the long-range cation order and enhances the stability of the cubic phase, which was also observed for other mixed hybrid perovskite systems.[24,32−34]

The same experiments of $FAPbBr_3$ revealed five distinct anomalies (see Figures 1 and S4) that correspond to two symmetry lowering (at 262 and 153 K) and three isostructural (182, 161, and 120 K) transitions, as discussed in refs 30, 42. Ultrasonic measurements also revealed an additional anomaly at about 140 K, which was not observed previously. Upon a decrease in x, the isostructural anomalies completely disappear, while those corresponding to the symmetry change remain but are shifted to lower temperature (Figure 1). The same transition behavior was also observed in a recent study of mixed $FA_{1-x}Cs_xPbX_3$ perovskites,[30] where it was hypothesized that the lattice deformation due to smaller Cs^+ cations disrupts the long-range FA cation interactions, leading to a complete suppression of the isostructural transitions. Given that the MA cation is also smaller than FA, a similar mechanism seems also plausible in $MA_{1-x}FA_xPbBr_3$.

At the intermediate value of mixing (x = 0.5), the transition anomalies in C_p and DSC data occur at about 167 and 129 K, but are very broad and poorly resolved (Figure 1). An additional anomaly occurs at 195 K, but it is only observed in the ultrasonic (Figure S4) and dielectric (see below) measurements. The origin of this anomaly is currently unknown. Note that the PXRD measurements (Figure S2) did not reveal any secondary unmixed phases of this compound.

We also performed temperature-dependent single-crystal XRD measurements to investigate the phase transitions and phase symmetry. The temperature dependence of the lattice parameters is shown in Figure S5, revealing transition anomalies for $x \leqslant 0.35$ compositions. With increasing FA content, the lattice deformation weakens, and for $x > 0.35$, the sharp anomalies vanish. However, the pseudocubic lattice constant changes the slope at some of the expected transition points. The compositions with high x, starting from x = 0.5, behave similarly to pure $FAPbBr_3$, where the distortions of the inorganic framework are weak. For all compositions, the cubic to tetragonal symmetry lowering produces additional diffraction intensities at halved (0.5h)kl [h(0.5k)l, hk(0.5l)] cubic layers, which testify the translational symmetry change to larger tetragonal unit cells (see Figure S6). Tetragonal to orthorhombic transitions in low x materials brings additional well-resolved splitting of diffraction peaks due to the further deformation of the crystal lattice. For high x concentrations, only weakening of the intensity of tetragonal peaks is observed as a result of further symmetry reduction. Figure S6 illustrates the hk0 and hk0.5 reciprocal lattices at 100 K, whereas Figure S7 shows the differences in hk1.5 layers for x = 0.35, 0.5, and 0.65 at various temperatures.

In general, the crystal structure analysis of low-temperature phases of $MAPbBr_3$ and $FAPbBr_3$ poses many difficulties due to the complex domain structure that appears with symmetry lowering. Additionally, a slight disturbance of the inorganic scaffold in response to amine ordering does not have a weighty influence on the intensities of the main cubic peaks. In the case of $FAPbBr_3$, the distortions of the structure under successive phase transitions are so small that the real model of the low-temperature phases was established using high-resolution powder X-ray synchrotron data,[39] and then it was confirmed by neutron diffraction and DFT studies.[41] Conventional single-crystal X-ray diffraction led to an averaged picture of much higher symmetry.[47] The same applies to $MAPbBr_3$ crystals, in which the structures of low-temperature phases were established based on synchrotron PXRD and neutron diffraction (see e.g., refs 48, 49). Thus, in the present study, we used single-crystal XRD only to probe the symmetry lowering via detection of the additional diffraction intensities, as a solution of the crystal structures is beyond the resolution of our accessible methods.

We used our experimental data together with the information provided in the literature[35−37,41,42] to construct the temperature−composition phase diagram of $MA_{1-x}FA_xPbBr_3$ (see Figure 2). The MA-rich region of the phase diagram is in qualitative agreement with the phase

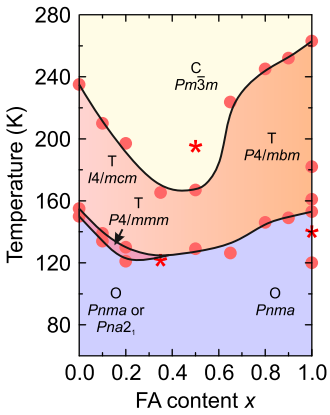

Figure 2. Temperature−composition phase diagram of mixed $MA_{1-x}FA_xPbBr_3$ perovskite showing cubic (C), tetragonal (T), and orthorhombic (O) phases. The dots indicate transition points detected by the majority of different experimental techniques, while asterisks mark anomalies that only occur in some of the experiments. The curves indicate tentative interpolation of the phase boundaries.

https://doi.org/10.1021/acs.chemmater.1c00885
Chem. Mater. 2021, 33, 5926−5934

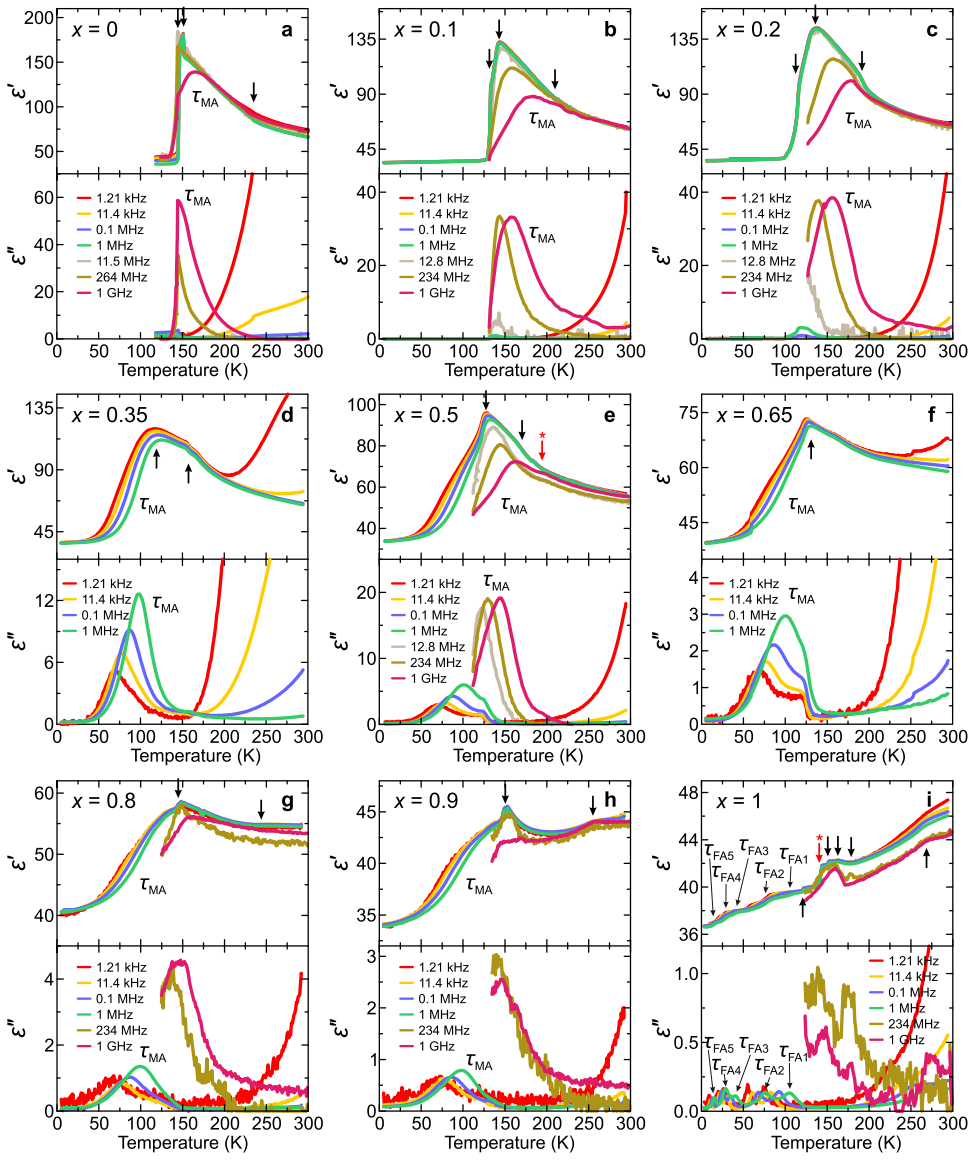

Figure 3. (a–i) Temperature dependence of the complex dielectric permittivity of $MA_{1-x}FA_xPbBr_3$ single crystals presented at selected frequencies. The arrows indicate phase transition anomalies.

diagrams reported for the related $MA_{1-x}FA_xPbI_3$ perovskite system.[33,34] However, the central part of our diagram is in contrast to the study by Francisco-López et al.,[33] where the tetragonal instead of an orthorhombic symmetry was found for $x > 0.4$ at low temperature. On the other hand, for the same iodide system, Mohanty et al.[34] observed a cubic superstructure for $x > 0.2$ below about 250 K. We did not observe such a superstructure in our system.

We investigated the molecular cation dynamics in the different regions of the phase diagram by performing broadband dielectric spectroscopy experiments. The dielectric data of the $MAPbBr_3$ sample is already reported by us in ref 24. The temperature dependence of the complex dielectric permittivity $\varepsilon^* = \varepsilon' - i\varepsilon''$ of this sample shows three phase transitions in agreement with other experiments (Figure 3a). The value of ε^* suddenly decreases at the tetragonal–orthorhombic phase transition point due to the cooperative ordering of the MA cations. The MA cation dynamics in the tetragonal and cubic phases are reflected in the frequency dependence of ε'', revealing a dipolar relaxation process in the GHz frequency range (Figure S8).

As x is increased to 0.1 and 0.2, the transition anomalies shift to lower temperature and become significantly broader (Figure 3b,c), although a step-like decrease of ε^* due to the MA cation ordering is still clearly visible. The frequency domain data show shifting of the dipolar relaxation to lower frequencies, indicating slowing down of MA cation dynamics (Figure S8). No relaxations are observed in the orthorhombic phase. For MA-rich samples, we expect a negligible contribution from the FA cations to the dielectric properties, as the electric dipole moment of FA is about an order of magnitude smaller than that of MA (0.21 vs 2.29 D).[11]

The dielectric response is different at the intermediate values of $0.35 \leq x \leq 0.65$, where the transition anomalies become very broad and barely resolvable (Figure 3d–f). Note the small kink-like anomalies in the dielectric data, some of which were also observed in the ultrasonic experiments (Figure S4). In addition, instead of a sudden decrease in ε^*, a dielectric dispersion is observed below 120 K. The frequency domain

https://doi.org/10.1021/acs.chemmater.1c00885
Chem. Mater. 2021, 33, 5926–5934

data of x = 0.5 composition (Figure S8) reveals that this process is a continuation of the MA cation relaxation to lower temperatures. This indicates a gradual freezing instead of a sudden ordering of the MA cations in contrast to the MA-rich compounds. The same MA relaxation is also observed for FA-rich samples (x = 0.8 and 0.9), although only in the low-temperature region (Figures 3g,h and S8). Two symmetry-breaking transitions inherited from $FAPbBr_3$ can be identified for these compositions in agreement with other experiments.

The dielectric response of the nonmixed $FAPbBr_3$ perovskite exhibits four additional anomalies (Figure 3i). Three of them can be related to the isostructural transitions (Figure 2),[30,42] while one observed at about 140 K is only present in the ultrasonic data (Figure S4). The overall temperature dependence of ε^* is in good agreement with the previous dielectric studies of the same compound.[39,47] In addition, five weak dipolar relaxations can be identified in the orthorhombic phase, which were previously poorly resolved and tentatively assigned to a glassy behavior.[39] Alternatively, the origin of these processes could be related to the freezing-out of charge carriers or dynamics of the FA cations. Note that the observed relaxations are absent in the mixed compounds.

A quantitative analysis of the frequency domain dielectric data allowed us to obtain the activation energies E_a of the observed dipolar processes in all studied compounds (see the Supporting Information for details). The obtained results are presented in Figure 4a, revealing more than a twofold increase

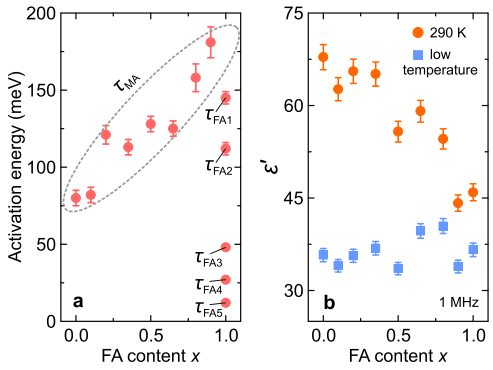

Figure 4. FA concentration dependence of (a) activation energy of the dipolar relaxations and (b) dielectric permittivity (1 MHz) obtained at 290 K and the lowest measured temperature.

in the E_a value (from 80(5) to 181(10) meV) of MA cation dynamics upon an increase in x. This indicates that the FA cations significantly raise the rotation barrier of the MA cations. On the other hand, the lattice expansion and deformation upon mixing prevent the cooperative ordering of the MA cations, resulting in the presence of their dynamics at much lower temperature than in nonmixed $MAPbBr_3$. Note that a similar behavior was also observed in a $MA_{1-x}DMA_xPbBr_3$ system.[24]

The activation energies of five low-temperature processes of $FAPbBr_3$ range from 145(4) to 12(1) meV (Figure 4a). Mozur et al.[30] used ^{1}H NMR to obtain E_a = 40 meV of FA cation dynamics in the orthorhombic phase of $FAPbBr_3$, while a higher value of 106 meV was determined in a recent quasi-elastic neutron scattering study.[50] Fabini et al.[51] found an FA rotation barrier of 84 meV in the low-temperature phase of the related $FAPbI_3$ perovskite. A wide range of the reported E_a values provides support for the assignment of the observed dielectric relaxations to the FA cation dynamics. In addition, such a distribution of energy barriers may be related to the recently proposed quadrupolar geometric frustration of the FA cations.[42] As discussed in ref 30, mixing relieves this frustration causing disappearance of the isostructural transitions, which might be connected to the absence of these low-temperature dipolar relaxations in the mixed compounds.

The MA and FA cation mixing significantly affects the dielectric permittivity of $MA_{1-x}FA_xPbBr_3$ perovskites, as revealed in Figure 3. The value of ε' in the cubic and tetragonal phases decreases upon an increase in x (Figure 4b), which is mainly determined by the diminishing number of the relaxing MA cations. The value of ε' obtained at low temperature, where cation relaxations are absent, is about 36 for all studied compounds. As recently discussed by Fabini et al.,[52] such a uniform and rather high value of ε' for different lead halide perovskites might be related to the lattice polarizability invoked by the $6s^2$ lone-pair electrons and associated off-centering of the lead cations.

The dipolar MA cation relaxation extending to low temperatures was also observed for the related $MA_{1-x}FA_xPbI_3$ system, where it was assigned to a dipolar glass phase, although no solid proof of such a behavior was provided.[34] To elucidate this, we analyzed the heat capacity data at low temperature. A signature of a glass phase is a higher heat capacity value and its deviation from the expected temperature dependence, which is typically revealed as a maximum in the C_p/T^3 representation.[53] Our experiments indicate such a maximum below 10 K, although it also occurs for the nonmixed compounds, indicating that it is not related to the mixing effects (Figure S10). An onset of another upturn is observed below 4 K only for the highly mixed $0.35 \leq x \leq 0.65$ compounds, providing a weak indication of a glassy phase. However, we did not observe any Vogel–Fulcher behavior[53] of the mean relaxation time (freezing of the dipolar glass) (Figure S9), although observation of this effect may require relaxation time measurements at much lower temperatures.

Strong signatures of the dipolar glass were previously observed in mixed $MA_{1-x}DMA_xPbBr_3$[24] and $MA_{1-x}Cs_xPbBr_3$[32] perovskites. These systems have DMA and Cs^+ cation solubility limits of about x = 0.3 and 0.4, respectively, indicating that the parent phases are less compatible compared to the $MA_{1-x}FA_xPbBr_3$, where no solubility limit exists. This suggests that the dipolar glass phase prefers and likely occurs in systems with strong local lattice distortions in agreement with our recent theoretical findings.[24]

We used the temperature-dependent Raman spectroscopy to further study the dynamic effects in $MA_{1-x}FA_xPbBr_3$ (x = 0, 0.1, 0.2, 0.5, 0.8, 0.9, and 1) perovskites and support our dielectric results. The Raman spectra were obtained in a 1020–420 cm^{-1} frequency range (Figure S10), which corresponds to the molecular vibrations (Figure S1).[33,54−56] The spectra of the MA-rich compounds exhibit drastic changes at the tetragonal–orthorhombic phase transitions in both frequency ranges, while the spectra of the $x \geq 0.5$ samples are less affected.

To investigate the Raman results in more detail, we determined the temperature dependence of the wavenumbers and full-width at half-maximum (FWHM) of the ν(CN)(MA), $\rho(NH_3)$ + $\rho(CH_3)$(MA), and δ(NCN)(FA) Raman bands (Figures 5 and S11). These parameters for the $MAPbBr_3$ sample show sharp transition anomalies at the expected phase transition points (Figure 5a,b,d,e). The FWHM of the $\rho(NH_3)$

https://doi.org/10.1021/acs.chemmater.1c00885
Chem. Mater. 2021, 33, 5926−5934

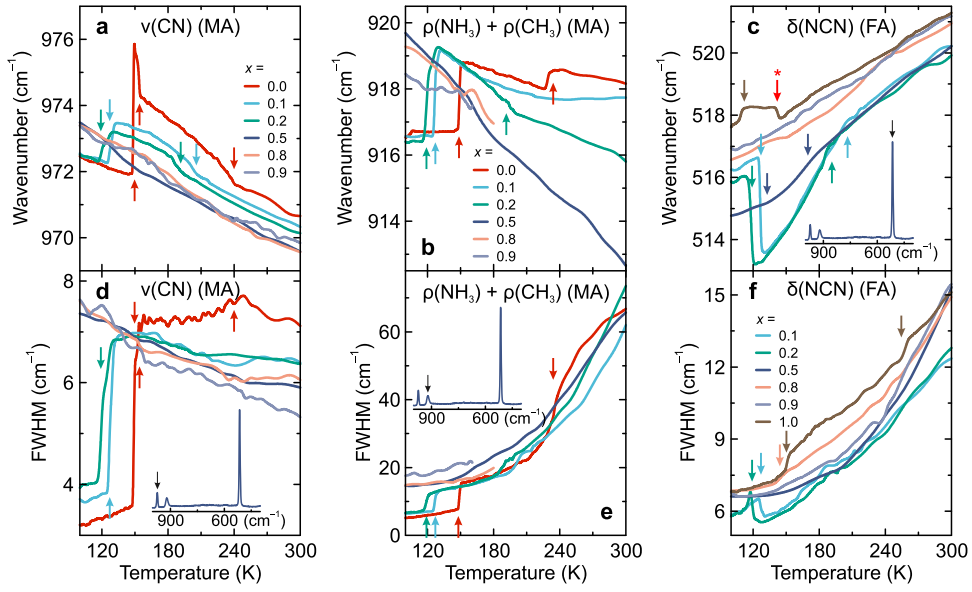

Figure 5. Temperature dependence of the (a−c) wavenumber and (d−f) FWHM of Raman bands corresponding to the (a, d) ν(CN)(MA), (b, e) $\rho(NH_3)$ + $\rho(CH_3)$(MA), and (c, f) δ(NCN)(FA) molecular vibrations in $MA_{1-x}FA_xPbBr_3$ perovskites. The arrows indicate phase transition anomalies. The corresponding bands are marked in the Raman spectrum (x = 0.5) presented in the insets.

+ $\rho(CH_3)$ band significantly decreases as temperature is decreased, indicating slowing down of the cation dynamics, while at the transition to the orthorhombic phase, the widths of both MA bands abruptly narrow, indicating ordering of the cations. The MA modes of the x = 0.1 and 0.2 samples demonstrate a similar behavior with broader and shifted anomalies in agreement with other experiments. Both parameters of the δ(NCN)(FA) mode exhibit anomalies, indicating that the FA cations are also affected by the transitions (Figure 5c,f). In addition, the cations also slow down with decreasing temperature, as indicated by the FWHM behavior of this mode. A small increase in the FWHM at the tetragonal−orthorhombic transition is likely related to splitting of this mode into bands of very similar wavenumbers that are not resolved in our experiment.

For the highest degree of mixing (x = 0.5), the MA modes do not exhibit any anomalous behavior, while the wavenumber of the FA band shows very weak changes in agreement with other experiments. The temperature dependences of the FWHM of the MA modes demonstrate a similar trend as for x = 0.1 and 0.2 compounds. However, the bands do not exhibit any substantial narrowing at low temperature, indicating the absence of the MA cation ordering. This is in good agreement with the dielectric spectroscopy results, which show pronounced dielectric relaxation of the MA cations at low temperature. The width of the FA band also decreases with decreasing temperature, indicating slowing down of the FA cation dynamics.

The FA-rich compositions (x = 0.8 and 0.9) show no clear anomalies, meaning that the cation−framework interactions are weakly affected by the phase transitions. The behavior of the ν(CN)(MA) band is very similar to the x = 0.5 case, while the $\rho(NH_3)$ + $\rho(CH_3)$(MA) mode is only resolved below about 180 K (Figure S11). The low-temperature limit of the FWHM of the latter mode is highest among all mixed compositions, indicating the highest degree of the MA cation disorder. The FA mode behaves similarly to the x = 0.5 case, suggesting comparable FA cation dynamics.

The FWHM of the FA band of the nonmixed $FAPbBr_3$ compound shows two anomalies at both symmetry-lowering transitions. In addition, the wavenumber of the same mode exhibits changes at about 140 and 120 K. The former anomaly was also observed in the ultrasonic and dielectric measurements (Figures 3 and S4), while the latter one corresponds to one of the previously reported isostructural transitions, confirming its relation to the FA cations.[30,42] This compound also shows the highest value of the FWHM of the FA band compared to all studied compositions. This indicates the highest degree of the FA cation disorder, which is surprisingly decreased by mixing. This observation is in agreement with the study of the $FA_{1-x}Cs_xPbBr_3$ system, where mixing was found to relieve the geometric FA cation frustration.[30] Note that other studies also observed a significant FA cation disorder at low temperatures in $FAPbBr_3$ and $FAPbI_3$ perovskites.[41,42,51]

SUMMARY AND CONCLUSIONS

We used a set of experimental techniques to explore the phase diagram and molecular cation dynamics of mixed $MA_{1-x}FA_xPbBr_3$ hybrid perovskites. The C_p, DSC, and ultrasonic experiments revealed a downshift of the phase transition temperatures and the increased stability of the region of the cubic phase upon mixing. Our XRD experiments showed weak symmetry lowering for the highest mixing level (x = 0.5). We also observed a complete suppression of the isostructural transitions of $FAPbBr_3$ even at the lowest MA concentration.

Our observations are consistent with the formation of a well-mixed solid solution of A-site cations. While local strain is invariably present due to the mismatch in molecular shape and size and gives rise to the dipole frustration, the effective mixing limits the emergence of macroscopic strain gradients. The result is a robust system that stabilizes isotropic crystal behavior. These effects underpin the application of mixed MA/FA perovskites in high-performance optoelectronic devices.

We used the broad-band dielectric and Raman spectroscopies to probe the dynamics of MA and FA cations in all studied compounds. The dielectric spectra of the MA-rich

https://doi.org/10.1021/acs.chemmater.1c00885
Chem. Mater. 2021, 33, 5926−5934

perovskites revealed a broadening of the transition anomalies, although the long-range MA cation order is still forming in these compounds. For the intermediate compositions, the transition anomalies were barely detected, and the dielectric relaxation corresponding to the MA cation dynamics extended to the low-temperature region. This indicates a gradual slowing down and freezing of the MA cation dynamics instead of a sudden ordering. A similar situation was also observed for the FA-rich compositions. The analysis of the dielectric data allowed us to extract the activation energies of the MA cation motion, indicating a gradual increase of the rotation barrier with the increasing FA concentration and MA cation disorder. The dielectric permittivity of $FAPbBr_3$ revealed several phase transitions in agreement with other experiments. In addition, five well-resolved dielectric relaxations were observed below 120 K, which were tentatively assigned to the quadrupolar frustration-affected FA cation dynamics; however, a separate study is required to unambiguously determine the origin of these low-temperature processes.

We also observed a significant decrease in the room-temperature dielectric permittivity value upon an increase in x. This effect is mainly related to a much smaller electric dipole moment of FA compared to a MA cation. The permittivity value at low temperature, where the cation dynamics is absent, remains rather high ($\varepsilon' \sim 36$). This observation supports the model,[52] where the lattice polarizability is invoked by the lone-pair electrons of the lead cations.

In addition, the low-temperature C_p data revealed weak signatures of the dipolar glass phase formation for the intermediate mixing levels ($0.35 \leq x \leq 0.65$). A comparison with other mixed perovskites, which show stronger evidence of such a phase formation, suggests that the dipolar glass phase occurs in systems that exhibit a high degree of local lattice distortions, which, in turn, lead to a more severe frustration of the electric dipoles.

The temperature-dependent Raman spectroscopy of the MA and FA modes revealed anomalies at the expected phase transition points in agreement with other experiments. More importantly, it allowed us to probe the FA cation dynamics in the mixed compositions, as such information is hardly accessible by dielectric spectroscopy due to a dominant response of the MA cations. The linewidth of the δ(NCN)-(FA) mode revealed slowing down of the FA cation dynamics with decreasing temperature. Surprisingly, the linewidth of the same mode was found to be the largest for the nonmixed $FAPbBr_3$ perovskite, indicating the highest degree of disorder of the FA cations. This observation supports the idea that mixing lifts a quadrupolar FA cation frustration, as observed in the $FA_{1-x}Cs_xPbBr_3$ system.[30]

■ ASSOCIATED CONTENT

Supporting Information

The Supporting Information is available free of charge at https://pubs.acs.org/doi/10.1021/acs.chemmater.1c00885.

Room-temperature powder XRD patterns, room-temperature light absorption spectra, ultrasonic velocity and attenuation data, additional single-crystal XRD, and dielectric, Raman, and heat capacity data (PDF)

■ AUTHOR INFORMATION

Corresponding Author

Mantas Šimėnas − *Faculty of Physics, Vilnius University, LT-10257 Vilnius, Lithuania;* orcid.org/0000-0002-2733-2270; Email: mantas.simenas@ff.vu.lt

Authors

Sergejus Balčiūnas − *Faculty of Physics, Vilnius University, LT-10257 Vilnius, Lithuania*

Šarūnas Svirskas − *Faculty of Physics, Vilnius University, LT-10257 Vilnius, Lithuania*

Martynas Kinka − *Faculty of Physics, Vilnius University, LT-10257 Vilnius, Lithuania*

Maciej Ptak − *Institute of Low Temperature and Structure Research, Polish Academy of Sciences, PL-50-422 Wroclaw, Poland*

Vidmantas Kalendra − *Faculty of Physics, Vilnius University, LT-10257 Vilnius, Lithuania*

Anna Gągor − *Institute of Low Temperature and Structure Research, Polish Academy of Sciences, PL-50-422 Wroclaw, Poland*

Daria Szewczyk − *Institute of Low Temperature and Structure Research, Polish Academy of Sciences, PL-50-422 Wroclaw, Poland*

Adam Sieradzki − *Department of Experimental Physics, Wroclaw University of Science and Technology, PL-50-370 Wroclaw, Poland;* orcid.org/0000-0003-4136-5754

Robertas Grigalaitis − *Faculty of Physics, Vilnius University, LT-10257 Vilnius, Lithuania*

Aron Walsh − *Thomas Young Centre and Department of Materials, Imperial College London, SW7 2AZ London, U.K.; Department of Materials Science and Engineering, Yonsei University, 03722 Seoul, Korea;* orcid.org/0000-0001-5460-7033

Mirosław Mączka − *Institute of Low Temperature and Structure Research, Polish Academy of Sciences, PL-50-422 Wroclaw, Poland*

Jūras Banys − *Faculty of Physics, Vilnius University, LT-10257 Vilnius, Lithuania*

Complete contact information is available at: https://pubs.acs.org/10.1021/acs.chemmater.1c00885

Notes

The authors declare no competing financial interest.

■ ACKNOWLEDGMENTS

This project has been funded by the Research Council of Lithuania (LMTLT) (agreement No. S-MIP-19-4).

■ REFERENCES

(1) Snaith, H. J. Perovskites: The Emergence of a New Era for Low-Cost, High-Efficiency Solar Cells. *J. Phys. Chem. Lett.* **2013**, *4*, 3623−3630.

(2) Grätzel, M. The Light and Shade of Perovskite Solar Cells. *Nat. Mater.* **2014**, *13*, 838−842.

(3) Stranks, S. D.; Snaith, H. J. Metal-Halide Perovskites for Photovoltaic and Light-Emitting Devices. *Nat. Nanotechnol.* **2015**, *10*, 391−402.

(4) Kojima, A.; Teshima, K.; Shirai, Y.; Miyasaka, T. Organometal Halide Perovskites as Visible-Light Sensitizers for Photovoltaic Cells. *J. Am. Chem. Soc.* **2009**, *131*, 6050−6051.

(5) Lee, M. M.; Teuscher, J.; Miyasaka, T.; Murakami, T. N.; Snaith, H. J. Efficient Hybrid Solar Cells Based on Meso-Superstructured Organometal Halide Perovskites. *Science* **2012**, *338*, 643−647.

(6) Burschka, J.; Pellet, N.; Moon, S.-J.; Humphry-Baker, R.; Gao, P.; Nazeeruddin, M. K.; Grätzel, M. Sequential Deposition as a Route to High-Performance Perovskite-Sensitized Solar Cells. *Nature* **2013**, *499*, 316−319.
(7) Park, N.-G. Organometal Perovskite Light Absorbers Toward a 20% Efficiency Low-Cost Solid-State Mesoscopic Solar Cell. *J. Phys. Chem. Lett.* **2013**, *4*, 2423−2429.
(8) Zhou, H.; Chen, Q.; Li, G.; Luo, S.; Song, T.-b.; Duan, H.-S.; Hong, Z.; You, J.; Liu, Y.; Yang, Y. Interface Engineering of Highly Efficient Perovskite Solar Cells. *Science* **2014**, *345*, 542−546.
(9) Li, Z.; Klein, T. R.; Kim, D. H.; Yang, M.; Berry, J. J.; van Hest, M. F. A. M.; Zhu, K. Scalable Fabrication of Perovskite Solar Cells. *Nat. Rev. Mater.* **2018**, *3*, No. 18017.
(10) Manser, J. S.; Christians, J. A.; Kamat, P. V. Intriguing Optoelectronic Properties of Metal Halide Perovskites. *Chem. Rev.* **2016**, *116*, 12956−13008.
(11) Frost, J. M.; Butler, K. T.; Brivio, F.; Hendon, C. H.; van Schilfgaarde, M.; Walsh, A. Atomistic Origins of High-Performance in Hybrid Halide Perovskite Solar Cells. *Nano Lett.* **2014**, *14*, 2584−2590.
(12) Stranks, S. D.; Eperon, G. E.; Grancini, G.; Menelaou, C.; Alcocer, M. J. P.; Leijtens, T.; Herz, L. M.; Petrozza, A.; Snaith, H. J. Electron-Hole Diffusion Lengths Exceeding 1 Micrometer in an Organometal Trihalide Perovskite Absorber. *Science* **2013**, *342*, 341−344.
(13) Chen, T.; Chen, W.-L.; Foley, B. J.; Lee, J.; Ruff, J. P. C.; Ko, J. Y. P.; Brown, C. M.; Harriger, L. W.; Zhang, D.; Park, C.; et al. Origin of Long Lifetime of Band-Edge Charge Carriers in Organic-Inorganic Lead Iodide Perovskites. *Proc. Natl. Acad. Sci. U.S.A.* **2017**, *114*, 7519−7524.
(14) Miyata, A.; Mitioglu, A.; Plochocka, P.; Portugall, O.; Wang, J. T.-W.; Stranks, S. D.; Snaith, H. J.; Nicholas, R. J. Direct Measurement of the Exciton Binding Energy and Effective Masses for Charge Carriers in Organic-Inorganic Tri-Halide perovskites. *Nat. Phys.* **2015**, *11*, No. 582.
(15) Ball, J. M.; Petrozza, A. Defects in Perovskite-Halides and their Effects in Solar Cells. *Nat. Energy* **2016**, *1*, No. 16149.
(16) Jeon, N. J.; Noh, J. H.; Yang, W. S.; Kim, Y. C.; Ryu, S.; Seo, J.; Seok, S. I. Compositional Engineering of Perovskite Materials for High-Performance Solar Cells. *Nature* **2015**, *517*, 476.
(17) Zhou, Y.; Zhou, Z.; Chen, M.; Zong, Y.; Huang, J.; Pang, S.; Padture, N. P. Doping and Alloying for Improved Perovskite Solar Cells. *J. Mater. Chem. A* **2016**, *4*, 17623−17635.
(18) Niemann, R. G.; Gouda, L.; Hu, J.; Tirosh, S.; Gottesman, R.; Cameron, P. J.; Zaban, A. Cs^+ Incorporation Into lceCH3NH3PbI3 Perovskite: Substitution Limit and Stability Enhancement. *J. Mater. Chem. A* **2016**, *4*, 17819−17827.
(19) Ono, L. K.; Juarez-Perez, E. J.; Qi, Y. Progress on Perovskite Materials and Solar Cells with Mixed Cations and Halide Anions. *ACS Appl. Mater. Interfaces* **2017**, *9*, 30197−30246.
(20) Boyd, C. C.; Cheacharoen, R.; Leijtens, T.; McGehee, M. D. Understanding Degradation Mechanisms and Improving Stability of Perovskite Photovoltaics. *Chem. Rev.* **2019**, *119*, 3418−3451.
(21) Saliba, M.; Matsui, T.; Domanski, K.; Seo, J.-Y.; Ummadisingu, A.; Zakeeruddin, S. M.; Correa-Baena, J.-P.; Tress, W. R.; Abate, A.; Hagfeldt, A.; et al. Incorporation of Rubidium Cations Into Perovskite Solar Cells Improves Photovoltaic Performance. *Science* **2016**, *354*, 206−209.
(22) Pei, Y.; Liu, Y.; Li, F.; Bai, S.; Jian, X.; Liu, M. Unveiling Property of Hydrolysis-Derived $DMAPbI_3$ for Perovskite Devices: Composition Engineering, Defect Mitigation, and Stability Optimization. *iScience* **2019**, *15*, 165−172.
(23) Anelli, C.; Chierotti, M. R.; Bordignon, S.; Quadrelli, P.; Marongiu, D.; Bongiovanni, G.; Malavasi, L. Investigation of Dimethylammonium Solubility in $MAPbBr_3$ Hybrid Perovskite: Synthesis, Crystal Structure, and Optical Properties. *Inorg. Chem.* **2019**, *58*, 944−949.
(24) Simenas, M.; Balciunas, S.; Wilson, J. N.; Svirskas, S.; Kinka, M.; Garbaras, A.; Kalendra, V.; Gagor, A.; Szewczyk, D.; Sieradzki, A.; et al. Suppression of Phase Transitions and Glass Phase Signatures in Mixed Cation Halide Perovskites. *Nat. Commun.* **2020**, *11*, No. 5103.
(25) Maczka, M.; Ptak, M.; Gagor, A.; Stefanska, D.; Zareba, J. K.; Sieradzki, A. Methylhydrazinium Lead Bromide: Noncentrosymmetric Three-Dimensional Perovskite with Exceptionally Large Framework Distortion and Green Photoluminescence. *Chem. Mater.* **2020**, *32*, 1667−1673.
(26) Maczka, M.; Gagor, A.; Zareba, J. K.; Stefanska, D.; Drozd, M.; Balciunas, S.; Simenas, M.; Banys, J.; Sieradzki, A. Three-Dimensional Perovskite Methylhydrazinium Lead Chloride with Two Polar Phases and Unusual Second-Harmonic Generation Bistability above Room Temperature. *Chem. Mater.* **2020**, *32*, 4072−4082.
(27) Binek, A.; Hanusch, F. C.; Docampo, P.; Bein, T. Stabilization of the Trigonal High-Temperature Phase of Formamidinium Lead Iodide. *J. Phys. Chem. Lett.* **2015**, *6*, 1249−1253.
(28) Charles, B.; Dillon, J.; Weber, O. J.; Islam, M. S.; Weller, M. T. Understanding the Stability of Mixed A-Cation Lead Iodide Perovskites. *J. Mater. Chem. A* **2017**, *5*, 22495−22499.
(29) Jesper Jacobsson, T.; Correa-Baena, J.-P.; Pazoki, M.; Saliba, M.; Schenk, K.; Grätzel, M.; Hagfeldt, A. Exploration of the Compositional Space for Mixed Lead Halogen Perovskites for High Efficiency Solar Cells. *Energy Environ. Sci.* **2016**, *9*, 1706−1724.
(30) Mozur, E. M.; Hope, M. A.; Trowbridge, J. C.; Halat, D. M.; Daemen, L. L.; Maughan, A. E.; Prisk, T. R.; Grey, C. P.; Neilson, J. R. Cesium Substitution Disrupts Concerted Cation Dynamics in Formamidinium Hybrid Perovskites. *Chem. Mater.* **2020**, *32*, 6266−6277.
(31) Charles, B.; Weller, M. T.; Rieger, S.; Hatcher, L. E.; Henry, P. F.; Feldmann, J.; Wolverson, D.; Wilson, C. C. Phase Behavior and Substitution Limit of Mixed Cesium-Formamidinium Lead Triiodide Perovskites. *Chem. Mater.* **2020**, *32*, 2282−2291.
(32) Mozur, E. M.; Maughan, A. E.; Cheng, Y.; Huq, A.; Jalarvo, N.; Daemen, L. L.; Neilson, J. R. Orientational Glass Formation in Substituted Hybrid Perovskites. *Chem. Mater.* **2017**, *29*, 10168−10177.
(33) Francisco-López, A.; Charles, B.; Alonso, M. I.; Garriga, M.; Campoy-Quiles, M.; Weller, M. T.; Goñi, A. R. Phase Diagram of Methylammonium/Formamidinium Lead Iodide Perovskite Solid Solutions from Temperature-Dependent Photoluminescence and Raman Spectroscopies. *J. Phys. Chem. C* **2020**, *124*, 3448−3458.
(34) Mohanty, A.; Swain, D.; Govinda, S.; Row, T. N. G.; Sarma, D. D. Phase Diagram and Dielectric Properties of $MA_{1-x}FA_xPbI_3$. *ACS Energy Lett.* **2019**, *4*, 2045−2051.
(35) Onoda-Yamamuro, N.; Matsuo, T.; Suga, H. Calorimetric and IR Spectroscopic Studies of Phase Transitions in Methylammonium Trihalogenoplumbates (II). *J. Phys. Chem. Solids* **1990**, *51*, 1383−1395.
(36) Onoda-Yamamuro, N.; Matsuo, T.; Suga, H. Dielectric Study of $CH_3NH_3PbX_3$ (X = Cl, Br, I). *J. Phys. Chem. Solids* **1992**, *53*, 935−939.
(37) Mashiyama, H.; Kawamura, Y.; Kubota, Y. The Anti-Polar Structure of $CH_3NH_3PbBr_3$. *J. Korean Phys. Soc.* **2007**, *51*, 850−853.
(38) Anusca, I.; Balčī ūnas, S.; Gemeiner, P.; Svirskas, S.; Sanlialp, M.; Lackner, G.; Fettkenhauer, C.; Belovickis, J.; Samulionis, V.; Ivanov, M.; et al. Dielectric Response: Answer to Many Questions in the Methylammonium Lead Halide Solar Cell Absorbers. *Adv. Energy Mater.* **2017**, *7*, No. 1700600.
(39) Schueller, E. C.; Laurita, G.; Fabini, D. H.; Stoumpos, C. C.; Kanatzidis, M. G.; Seshadri, R. Crystal Structure Evolution and Notable Thermal Expansion in Hybrid Perovskites Formamidinium Tin Iodide and Formamidinium Lead Bromide. *Inorg. Chem.* **2018**, *57*, 695−701.
(40) Keshavarz, M.; Ottesen, M.; Wiedmann, S.; Wharmby, M.; Küchler, R.; Yuan, H.; Debroye, E.; Steele, J. A.; Martens, J.; Hussey, N. E.; et al. Tracking Structural Phase Transitions in Lead-Halide Perovskites by Means of Thermal Expansion. *Adv. Mater.* **2019**, *31*, No. 1900521.
(41) Franz, A.; Többens, D. M.; Lehmann, F.; Kärgell, M.; Schorr, S. The Influence of Deuteration on the Crystal Structure of Hybrid

Halide Perovskites: a Temperature-Dependent Neutron Diffraction Study of $FAPbBr_3$. *Acta Crystallogr. B* **2020**, *76*, 267−274.
(42) Mozur, E. M.; Trowbridge, J. C.; Maughan, A. E.; Gorman, M. J.; Brown, C. M.; Prisk, T. R.; Neilson, J. R. Dynamical Phase Transitions and Cation Orientation-Dependent Photoconductivity in $CH(NH_2)_2PbBr_3$. *ACS Mater. Lett.* **2019**, *1*, 260−264.
(43) Banys, J.; Lapinskas, S.; Rudys, S.; Greicius, S.; Grigalaitis, R. High Frequency Measurements of Ferroelecrics and Related Materials in Coaxial Line. *Ferroelectrics* **2011**, *414*, 64−69.
(44) Svirskas, Š.; Jablonskas, D.; Rudys, S.; Lapinskas, S.; Grigalaitis, R.; Banys, J. Broad-Band Measurements of Dielectric Permittivity in Coaxial Line Using Partially Filled Circular Waveguide. *Rev. Sci. Instrum.* **2020**, *91*, No. 035106.
(45) Grigas, J.; Brilingas, A.; Kalesinskas, V. Microwave and Millimetre Wave Dielectric Spectroscopy of Ferroelectrics. *Ferroelectrics* **1990**, *107*, 61−66.
(46) Salado, M.; Calio, L.; Berger, R.; Kazim, S.; Ahmad, S. Influence of the Mixed Organic Cation Ratio in Lead Iodide Based Perovskite on the Performance of Solar Cells. *Phys. Chem. Chem. Phys.* **2016**, *18*, 27148−27157.
(47) Govinda, S.; Kore, B. P.; Swain, D.; Hossain, A.; De, C.; Guru Row, T. N.; Sarma, D. D. Critical Comparison of $FAPbX_3$ and $MAPbX_3$ (X = Br and Cl): How Do They Differ? *J. Phys. Chem. C* **2018**, *122*, 13758−13766.
(48) López, C. A.; Martínez-Huerta, M. V.; Alvarez-Galván, M. C.; Kayser, P.; Gant, P.; Castellanos-Gomez, A.; Fernández-Díaz, M. T.; Fauth, F.; Alonso, J. A. Elucidating the Methylammonium (MA) Conformation in $MAPbBr_3$ Perovskite with Application in Solar Cells. *Inorg. Chem.* **2017**, *56*, 14214−14219.
(49) Yang, B.; Ming, W.; Du, M.-H.; Keum, J. K.; Puretzky, A. A.; Rouleau, C. M.; Huang, J.; Geohegan, D. B.; Wang, X.; Xiao, K. Real-Time Observation of Order-Disorder Transformation of Organic Cations Induced Phase Transition and Anomalous Photoluminescence in Hybrid Perovskites. *Adv. Mater.* **2018**, *30*, No. 1705801.
(50) Sharma, V. K.; Mukhopadhyay, R.; Mohanty, A.; Tyagi, M.; Embs, J. P.; Sarma, D. D. Contrasting Behaviors of FA and MA Cations in $APbBr_3$. *J. Phys. Chem. Lett.* **2020**, *11*, 9669−9679.
(51) Fabini, D. H.; Siaw, T. A.; Stoumpos, C. C.; Laurita, G.; Olds, D.; Page, K.; Hu, J. G.; Kanatzidis, M. G.; Han, S.; Seshadri, R. Universal Dynamics of Molecular Reorientation in Hybrid Lead Iodide Perovskites. *J. Am. Chem. Soc.* **2017**, *139*, 16875−16884.
(52) Fabini, D. H.; Seshadri, R.; Kanatzidis, M. G. The Underappreciated Lone Pair in Halide Perovskites Underpins Their Unusual Properties. *MRS Bull.* **2020**, *45*, 467−477.
(53) Höchli, U. T.; Knorr, K.; Loidl, A. Orientational Glasses. *Adv. Phys.* **1990**, *39*, 405−615.
(54) Brivio, F.; Frost, J. M.; Skelton, J. M.; Jackson, A. J.; Weber, O. J.; Weller, M. T.; Goñi, A. R.; Leguy, A. M. A.; Barnes, P. R. F.; Walsh, A. Lattice Dynamics and Vibrational Spectra of the Orthorhombic, Tetragonal, and Cubic Phases of Methylammonium Lead Iodide. *Phys. Rev. B* **2015**, *92*, No. 144308.
(55) Leguy, A. M. A.; Goñi, A. R.; Frost, J. M.; Skelton, J.; Brivio, F.; Rodríguez-Martínez, X.; Weber, O. J.; Pallipurath, A.; Alonso, M. I.; Campoy-Quiles, M.; et al. Dynamic Disorder, Phonon Lifetimes, and the Assignment of Modes to the Vibrational Spectra of Methylammonium Lead Halide Perovskites. *Phys. Chem. Chem. Phys.* **2016**, *18*, 27051−27066.
(56) Nakada, K.; Matsumoto, Y.; Shimoi, Y.; Yamada, K.; Furukawa, Y. Temperature-Dependent Evolution of Raman Spectra of Methylammonium Lead Halide Perovskites, $CH_3NH_3PbX_3$ (X = I, Br). *Molecules* **2019**, *24*, No. 626.

https://doi.org/10.1021/acs.chemmater.1c00885
Chem. Mater. 2021, 33, 5926−5934